Gallium Nitride Phononic Crystal Resonator

by

Siping Wang

B.S., Cornell University (2012)

Submitted to the Department of Electrical Engineering and Computer Science
in partial fulfillment of the requirements for the degree of

Master of Science

at the

MASSACHUSETTS INSTITUTE OF TECHNOLOGY

June 2015

Signature redacted

Author .....
Department of Electrical Engineering and Computer Science
April, 3 2015

Signature redacted

Certified by .....
Dana Weinstein
Associate Professor
Thesis Supervisor

Signature redacted

Accepted by .....
Leslie A. Kolodziejski
Chairman, Department Committee on Graduate Theses

Gallium Nitride Phononic Crystal Resonator

by

Siping Wang

Submitted to the Department of Electrical Engineering and Computer Science
on April, 3 2015, in partial fulfillment of the
requirements for the degree of
Master of Science

Abstract

We present a Gallium Nitride (GaN) Lamb Wave resonator using a Phononic Crystal (PnC) to selectively confine elastic vibrations with wide-band spurious mode suppression. A unique feature of the design demonstrated here is a folded PnC structure to relax energy confinement in the non-resonant dimension and to enable routing access of piezoelectric transducers inside the resonant cavity. This provides a clean spectrum over a wide frequency range and improves series resistance relative to transmission line or tethered resonators by allowing a low-impedance path for drive and sense electrodes. GaN resonators are demonstrated with wide-band suppression of spurious modes, $f \cdot Q$ product up to 3.06×10^{12}, and resonator coupling coefficient k^2_{eff} up to 0.23%. (filter BW up to 0.46%). Furthermore, these PnC GaN resonators exhibit record-breaking power handling, with IIP_3 of +27.2dBm demonstrated at 993MHz.

Thesis Supervisor: Dana Weinstein
Title: Associate Professor

Acknowledgments

My choice for graduate school was not an easy one, I was excited about so many subjects and I was not where to go and what to study. Now when looking back, I am glad I made the choice to join HybridMEMS group at MIT, where I met some many brilliant people, learned physics, MEMS, CS, electrical engineering, and more importantly learned how to conduct research, take on projects, work through all the difficulties and solve problems.

First, I would like to thank my adviser Professor Dana Weinstein. She provided the utmost support I can possibly expect as a graduate student, who is new to the field, excited but inexperienced. Dana's passion in MEMS gives me confidence in the various projects I am pursuing; she listens carefully and provides her help not only as a mentor, but also as a co-worker, when she spent hours in the lab, going through the measurement set up together with me. Her research proposals are no short of ingenuity and her vision is always a source of inspiration for new ideas. I feel I am always free to explore and try out new ideas, and Dana is always there to help, listen, provide you with support and idea.

Next, I would like to thank my group members: Laura Popa, Wentao Wang, Radhika Marathe, Bichoy Bahr, Subra Sundaram, Steven Ye, Bethany Kroese, Matt Storey and Tianyi Zheng. I learned so much and received tremendous help from each of you, whether it is about setting up the simulation correctly, conducting measurements using probe station, figuring out how to make a plan about the fabrication, taking SEM images, issues with drawing layout, bouncing out new ideas, trying to understand Phononic Crystal together and countless many others. I am grateful for your presence, proud to be part of this team and wish everyone of you best luck in your future career! I would also like to express my best wish for the youngest group member, Sophia Bhave. Watching you grow up is a real pleasure of mine.

I would also like to mention the great help I got from other faculties member in the MIT and Cornell communities, either through courses or various conversations and office hours. Professor Steven Johnson was instrumental in me trying to understand

the elegance in periodic structures and the art of manipulating waves. Professor Luca Daniel and Jacob White taught me numerical simulation, a powerful weapon for design and analysis, and absolutely necessary in understanding the simulation tools I have been using. Professor Terry Orlando taught me solid state physics and Professor Jeffery Lang taught me Electromagnetic waves, both subjects are of significant help to my research projects. Professor Sunil Bhave and Professor Paul McEuen introduced me to the field of MEMS and Microsystem while I was still an undergraduate at Cornell. It was my pleasure to have the chance to learn from real experts and innovators in this field.

I would also like to thank Brian Schultz and Thomas Kazior at Raytheon for GaN growth and process discussions. This work was funded by DRAPA DAHI Foundry N66001-13-1-4022 and NSF Career EECS-1150493.

Lastly, I would like to thank my families and friends. I miss you all very much. I am lucky to have everyone of you as part of my life. This thesis is dedicated to all of you.

Contents

Chapter 1

Introduction

1.1 Motivation

High Q, small footprint MEMS resonators are very promising for building blocks in RF wireless communication, timing, inertial navigation, and sensing applications. Their potential for monolithic integration with circuits provides critical benefits such as the elimination of parasitic capacitance and inductance from bond pads and off-chip routing, size, weight, and power scaling, and simplification of fabrication and packaging. This thesis aims to leverage the unique properties of Gallium Nitride and Phononic Crystal in improving the state of art MEMS resonator technology.

1.2 MEMS Resonator

Using mechanical resonators for RF signal processing has had a long history. They have been widely used in cellular communication, television and etc. I list the main categories as follows.

1.2.1 BAW and FBAR Resonators

Commercially available (Film Bulk Acoustic Resonator) FBARs are fabricated by depositing piezoelectric AlN thin-films sandwiched between metal (often Mo) trans-

duction electrodes on a sacrificial material such as silicon-dioxide. The AlN layer is patterned to define the boundaries and anchoring tethers of the resonator, and the sacrificial material is etched from underneath the acoustically active area to create a free-standing device. In Surface Mount Resonator (SMR) topologies, the metal/piezoelectric material/metal sandwich is deposited on an acoustic Bragg reflector stack. The reflector consists of alternating layers of nominally quarter wavelength thick high and low acoustic impedance materials. The number of such layers depends on the impedance ratio of the reflector materials and the desired reflection coefficient of the reflector. FBAR resonators have low motional impedance and high power handling. They are prevalent in filter systems in cellular communication system, but can not be defined lithographically to serve multiple frequencies on the same chip.

1.2.2 Surface Acoustic Wave (SAW) resonator

Surface acoustic wave (SAW) devices are ubiquitous as signal processing elements in communication system architectures and other electronic applications. The operation of these devices is based on traveling or standing Rayleigh waves along the surface of bulk piezoelectric substrates. The wavelength (and consequently frequency) of the surface wave is determined to first order by the period of the interdigitated transducer (IDT) electrodes. The acoustic path in SAW devices is often hundreds of acoustic wavelengths long, which can result in ungainly form factors, particularly for IF devices. Traditionally, the reliance of SAW devices on exotic bulk crystalline substrates has precluded monolithic integration with conventional circuitry.

1.2.3 Electrostatic MEMS Resonator

Bulk mode electrostatic MEMS resonators fabricated using Polysilicon or single-crystal silicon (SCS) device layer of silicon-on-insulator (SOI) wafers have been studied extensively The operation of these devices is based on driving either standing bulk longitudinal waves across some lateral dimension or shear waves across the thickness of an acoustically isolated structural plate. These structures are compatible with

system integration with circuits, but proves to be an inefficient driving mechanism, leading to low transduction coefficient and high motional impedance.

1.2.4 Contour Mode Piezoelectric resonator

Recently researchers have started investigating the potential of contour mode MEMS resonators in piezoelectric material platforms that can be more easily integrated with circuits, such that multiple frequencies can be defined on the same chip, since the resonator frequency is not limited by film thickness and can be defined lithographically. SAW resonators can be defined lithographically, but they usually require mm^2 scale footprint, much larger than a contour mode MEMS resonator (10-100 μm^2). Compared to electrostatic transduction, piezoelectric transduction is much more efficient, hence lower motional impedance and better integration with RF system, which has 50 Ω for input-output impedance.

1.3 GaN Technology

GaN has become the second most popular semiconductor after Silicon due to its excellent electrical property. With GaN's wide band gap (3.4 eV) and AlGaN/GaN heterostructure, GaN exhibits high 2DEG mobility, electron velocity and break down voltage, making it an ideal candidate for high power (>10 W/mm) and high frequency applications.

In addition, GaN also has great electromechanical properties, such as high piezoelectric coupling coefficient (electromechanical coupling k_T^2 up to 2% in FBAR-like structures) and low acoustic loss (resonator Q higher demonstrated above 5000).

Recent advances in GaN Monolithic Microwave IC (MMIC) technology have made it an attractive platform for the realization of high performance MEMS resonators. Compared to other piezoelectric material, GaN has the unique advantage of being able to be integrated with High Electron Mobility Transistors (HEMTs). This presents many opportunities for high power, high frequency applications.

1.4 Phononic Crystal

This work focuses on the development of MEMS resonators for channel-select filtering in RF receiver front ends. For a MEMS band pass filter, the presence of spurious modes in the constituent resonators strongly impacts filter performance. Resonators with a clean frequency spectrum help reduce ripples in the pass-band and prevent interference from unwanted signals outside the pass-band. Conventional MEMS resonator designs with free mechanical boundaries are inherently prone to spurious modes, since free boundaries act as acoustic reflectors over all frequencies. To resolve this issue, the resonator boundary needs to be frequency selective.

One way to define the MEMS resonator cavity with frequency selective confinement is by using Phononic Crystals (PnCs), which involve periodic scatters to achieve highly reflective boundary conditions only for frequencies in a specific range. This acoustic band gap can be engineered based on the unit cell size and material configuration. Research in micro-scale PnCs has progressed rapidly in the past decade with band gap optimization at GHz frequencies in Si and SiC [10] [5] and high-Q resonators in Si, AlN and ZnO [7] [6] [2]. High-Q resonant cavities using PnCs have been previously defined either as defect modes in a uniform 2D PnC (Fig. 1(a)) or as a suspended slab with free boundaries in the non-resonant dimension (Fig. 1(b)). While the acoustic band gap of these PnCs helps reduce resonance outside the band gap, these structures provide no spurious mode suppression inside the band gap. Furthermore, transducers must be routed through the PnC in these configurations, leading to resistive loading of Q.

In this work, we demonstrate a new resonant structure leveraging both PnC acoustic confinement and the electromechanical benefits of GaN. The proposed GaN folded PnC structure (1-1(c)) provides several important benefits:

1. wide-band spurious mode suppression, both outside and inside the PnC band gap, through relaxed confinement in the non-resonant dimension,

2. low-loss electrical routing to the resonant cavity to incorporate drive and sense transducers inside the resonator,

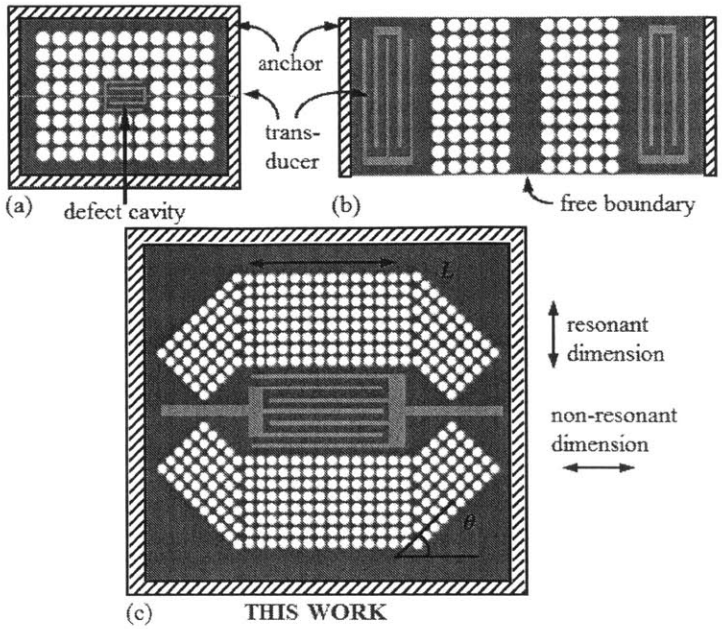

Figure 1-1: 3 types of PnC resonator configurations

3. improved heat dissipation relative to other PnC or tethered resonators, and

4. robust design that is immune to residual stress and handling. Using the folded PnC design, these improvements can be achieved while maintaining quality factor and transducer coupling comparable to traditional tethered resonators.

Chapter 2

Background

The background chapter aims to help readers understand the how MEMS resonator works and its various specifications. I will focus on the less obvious aspects, which I find not obvious. For a more thorough introduction of MEMS resonators, please refer to Dr. Phil Stephanou's PhD thesis [9] and Ville Kaajakari's Practical MEMS book [4]

2.1 MEMS Resonator Modeling

Motion equation:

$$m\frac{\partial^2 x}{\partial t^2} + b\frac{\partial x}{\partial t} + kx = F \tag{2.1}$$

RLC circuit equation:

$$L\frac{\partial^2 q}{\partial t^2} + R\frac{\partial q}{\partial t} + \frac{1}{C}q = V \tag{2.2}$$

Mapping between the electrical domain and mechanical domain:

$$L = \frac{m}{\eta^2} \tag{2.3}$$

$$C = \frac{\eta^2}{k} \tag{2.4}$$

$$R = \frac{b}{\eta^2} \tag{2.5}$$

, where is transduction coefficient η is defined as $\frac{F}{V}$.

$$\omega_o = \frac{1}{\sqrt{LC}} = \sqrt{\frac{k}{m}} \tag{2.6}$$

Quality factor Q can be written in the following form

$$Q = \frac{m\omega_o}{b} = \frac{1}{R\omega_o C} \tag{2.7}$$

$$Q = \frac{\sqrt{\frac{L}{C}}}{R} = \frac{\sqrt{mk}}{b} \tag{2.8}$$

For a given transducer configuration, namely C_m/C_o is determined by geometry and frequency, the relative peak height is directly related to quality factor Q, as can be proved easily, using Y11 for example

$$\text{Relative Peak Height} = \frac{\frac{V}{R}}{\frac{V}{1/(j\omega_o C_o)}} = \frac{1}{R\omega_o C_o} \propto \frac{\sqrt{\frac{L}{C}}}{R} \tag{2.9}$$

Simply making the structure larger by a factor α, assuming

- electrode or transducer configuration remains the same
- anchor loss is neglected

quality factor Q should not be affected, thus the relative peak height should remain the same. This is because:

$$Q = \frac{\sqrt{\alpha m \cdot \alpha k}}{\alpha b} = \frac{\sqrt{mk}}{b} \tag{2.10}$$

2.2 Resonator Coupling factor k^2_{eff}

The resonator coupling factor k^2_{eff} is defined as the ratio difference between the series resonance and parallel resonance in the measured frequency response.

$$k_{eff}^2 = 1 - \frac{\omega_s^2}{\omega_p^2} \tag{2.11}$$

Resonator coupling factor is an important device specification, since it is closely related to filter insertion loss and achievable bandwidth. It measures the efficiency that electric energy is converted to acoustic energy in the resonator. Quality factor Q, on the other hand, measures how well the resonator can retain its vibrational energy. Thus coupling factor k_{eff}^2 and Q can be thought as two orthogonal measures for the resonator performance, and the Figure of Merit (FOM) for acoustic/MEMS resonators can be defined as:

$$\text{FOM} = \frac{1 - k_{eff}^2}{k_{eff}^2} Q \tag{2.12}$$

when k_{eff}^2 is small compared to 1,

$$\text{FOM} \approx k_{eff}^2 Q \tag{2.13}$$

When using BVD model to represent an acoustic resonator, coupling factor is largely and fundamentally determined by the ratio between the motional capacitor and the feed through capacitor (c_m/c_o), but it is still subject to the influence of Q, when $k_{eff}^2 Q$ is not $\gg 1$.

An BVD model is used to investigate in what regime and how does k_{eff} depend on Q. As shown in the circuit diagram, C_m, C_o, L_m and R_m are chosen to give a series resonance at 1GHz, a capacitor ratio (c_m/c_o) of 0.05%. The motional impedance is varied to give variable quality factor in the range of 1000 to $10,000$.

As can be seen from Fig. (2-1), as quality factor Q increases, series (maximum of Y11)and parallel resonances (minimum of Y11) become gradually closer, leading to a decrease in k_{eff}^2. As Q increases and $k_{eff}^2 Q$ gets larger than 4, k_{eff}^2starts converging to its fundamental limit, $c_m/c_o = 0.05\%$. Despite of the trade off between Q and $k_{eff}^2$when Q is small, FOM is a monotonic function of Q, and keeps increasing as Q gets larger. c_m/c_o determines the fundamental limit of k_{eff}^2, which is subject to the

influence of Q when $k_{eff}^2 Q$ is small.

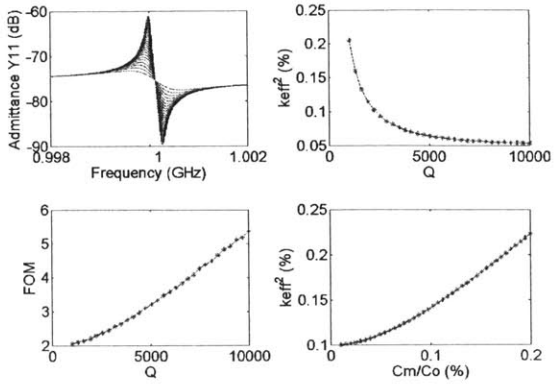

Figure 2-1: $k_{eff}^2$and FOM's dependence on c_m/c_o and resonator quality factor Q

2.3 Phononic Crystal

Phononic Crystal (PnC) refers to a structure with periodic variations in their mechanical properties, analogous to its photonic counterparts (PC), which has periodic variations in their electromagnetic properties. These structures have gained a lot of attention in recent years due to their unique frequency characteristics which are not seen in conventional bulk materials with uniform properties. As in any periodic structure, plane wave becomes a block wave and takes the following form in 1D :

$$u_k = u(x)e^{j(kx-\omega t)} \tag{2.14}$$

where $u(x)$ is a envelope function that has the same periodicity as the PnC. There are several very important implications. The first of them being that the dispersion relationship (ω vs k plot) becomes periodic in k space. The second important implication is the presence of a band gap, namely, there exists a frequency range, at which no wave can propagate through. Intuitively speaking, every location that the material property changes, the wave is scattered due to impedance mismatch. For frequencies in the band gap, the scatterings are in phase with each other and consequently all the energy is reflected, meaning no transmission or propagation. This is a

direct consequence of the periodic dispersion relationship, since if the ωvsk plot can extend to infinite k, there would not be any frequency gap.

To simulate the band structure and, more importantly, to get the band gap of the PnC, an eigenfrequency simulation is performed on the unit cell with floquet boundary conditions. A full list of eigenfrequencies of the unit cell is calculated at each $\vec{k}$. After a parametric sweep through all the $\vec{k}$ inside the Brillouin zone, a complete band structure for the PnC structure can be derived. For more details related to periodic structures, block waves, photonic crystals, please refer to following reference [3].

Chapter 3

Design and Simulation

This chapter explains the different considerations and various trade-offs in designing a folded PnC MEMS resonator. The sources of spurious modes, choice the PnC structure and specific choice of folding angle (θ) and cavity length (L) are discussed.

Fig. 3-1 illustrates the schematic of the folder PnC resonator, with folding angle θ, cavity length L, non-resonant dimension and resonant dimension labeled on the graph.

3.1 Spurious Modes

In the context of a MEMS resonator, spurious modes are unwanted vibrational modes, which will be excited along with the desired mode that the resonator is designed for to provide efficient frequency selection at the required frequency. One of the most common types of resonators made of piezoelectric materials like GaN is the lamb wave resonator, shown here with interdigitated (IDT) transducers. The lamb mode resonator is so popular because multiple resonance frequencies can be lithographically defined on a single chip. While this bar resonator is great at exciting the lamb mode (S_0), its overall filter performance suffers due to the disadvantage that it is also efficient at exciting a bunch of spurious modes, as shown in a typical frequency spectrum for such freely suspended resonator in Fig. ??.

Spurious modes exist because the resonance structure has infinite number of eigen-

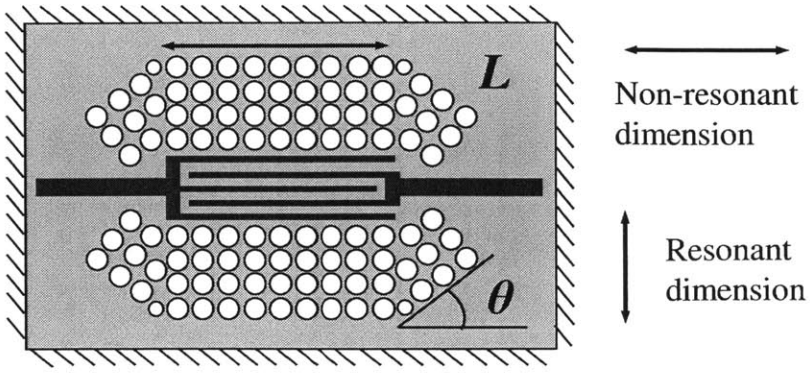

Figure 3-1: Simulated frequency spectrum for a typical free-boundary MEMS piezoelectric lamb wave mode resonator.

modes and the designed resonance mode is only one of the infinite many modes. Spurious modes will be detected on the sensing as long as the following conditions are met:

1. The spurious mode shape has nonzero overlap with the driving ans sensing transducers. In typical designs, driving ans sensing transducers have similar configuration for effective detection of the desired resonance mode. For one port devices, The same set of IDT transducer is used for both driving and sensing. This condition is equivalent to requiring that the transduction factor $\eta \neq 0$.

2. Vibrational energy of the spurious mode can be confined, namely quality factor $Q \neq 0$.

Researchers have tried to suppress the spurious modes by tweaking the resonator dimensions or using electrode patterning [1]. The first approach attempts to push the unwanted modes to frequencies far from the desired resonance, but can never completely eliminate the unwanted response and is irreproducible for a different geometry. On the other hand, electrode patterning attempts to overcome the first condition ($\eta \neq 0$) by reducing the overlap between the transducers and spurious modes. This approach often introduces complicated transducer design and electrode

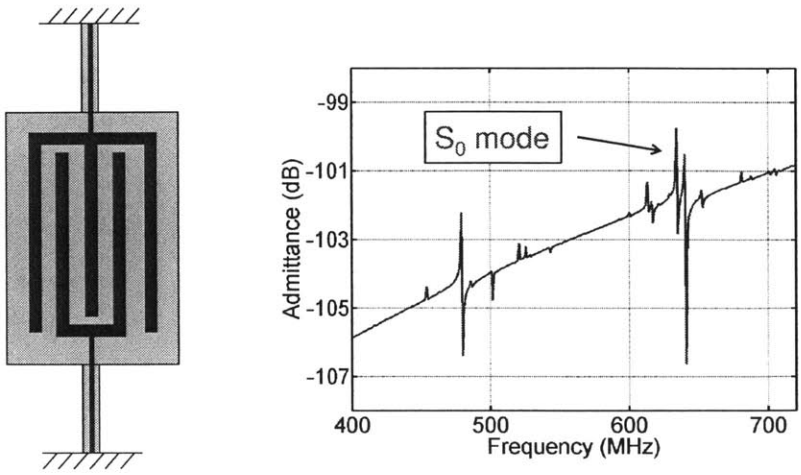

Figure 3-2: Simulated frequency spectrum for a typical free-boundary MEMS piezoelectric lamb wave contour mode bar resonator.

routing. Both approaches are limited by the specific geometry and mode shape of the resonator, limited to a relatively small frequency range and not capable of providing wide band spurious mode suppression. In response to the limitations for conventional spurious mode suppression techniques, a frequency selective boundary condition is proposed for spurious mode suppression. Namely, the resonator boundary is effective for energy confinement only around the desired mode's frequency, and serves as a leaky confinement for all other frequencies. Such kind of frequency selective boundary condition overcomes the second neccessary condition for spurious modes to exist. As shown in Chapter 2, band gap is one of the unique properties of periodic structures. Only waves at a certain frquency inside the bandgap can be reflected by the periodic structure, making PnC the perfct frequency selective boundary condition for spurious mode suppression.

3.2 Spurious Modes Inside the Bandgap

While the PnC resonator inherently suppresses spurious modes outside the band gap, it can still support resonance whose frequency happens to reside inside the band gap. Energy confinement along the non-resonant dimension must therefore be relaxed while

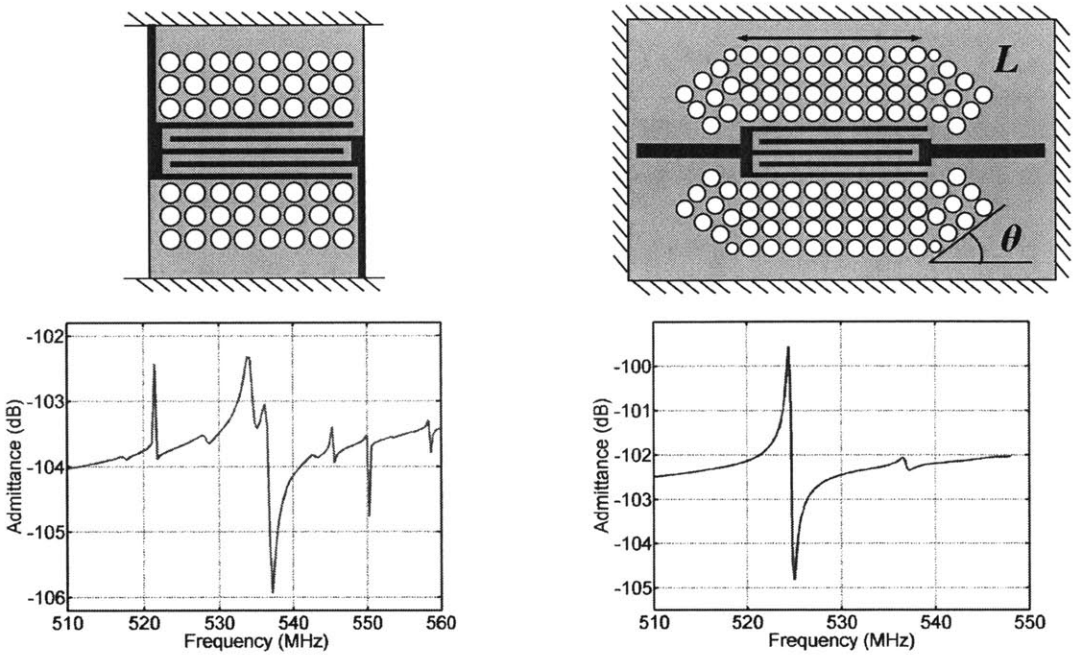

Figure 3-3: Simulated frequency spectrum of PnC resonators with free boundaries along the non-resonant dimension and PnC resonators with folder PnC structure.

maintaining high Q for the fundamental mode. These design considerations motivated the folded-PnC structure, in which square lattice PnC segments are designed at a folding angle θ relative to the main PnC to provide good confinement for the desired mode while minimizing standing waves formed in the non-resonant dimension by providing a leaky path along the non-resonant dimension. Fig. ?? shows the frequency spectrum of a PnC resonator with free boundaries along the non-resonant dimension and the frequency spectrum of that exact same structure, but with free boundary replaced by the the folded PnC structure.

For the folded PnC resonators, it was found that the majority of spurious modes found inside the band gap are due to harmonics established in the non-resonant dimension.

Fig. 3-4 shows the spurious peaks inside the band gap and their individual mode shapes, verifying that the spurious modes are due to standing wave patterns formed along the nonresonant dimension.

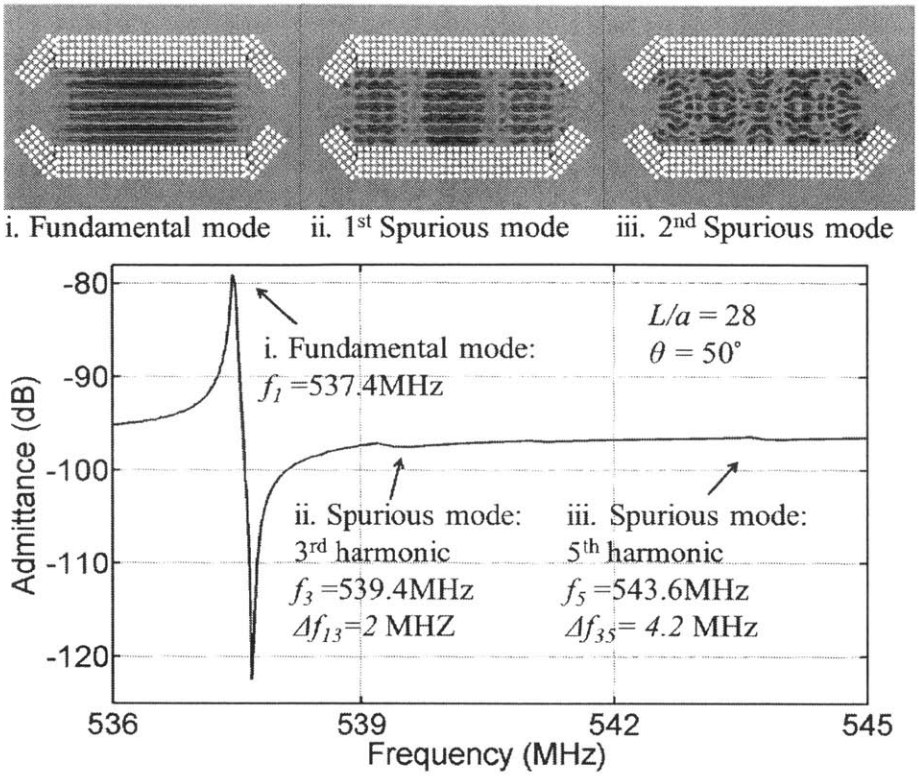

Figure 3-4: Simulated resonator mode shape and frequency spectrum. Compressive strain field along the resonant dimension is plotted.

3.3 PnC Selection

A square lattice PnC was chosen to define the resonant cavity of the folded PnC resonator. The PnC unit cell is a square block with a finite thickness defined by the GaN layer thickness, and a circular hole at the center as illustrated in Fig. 3-5(a). For the irreducible Brillouin zone (IBZ) in Fig. 3-5(b), the PnC band structure of the 537 MHz (unit cell a = 5.6 μm) resonators in this work is given in Fig. 3-5(c). It should be noted that the PnC does not have a complete band gap. Rather, there are only band gaps from O to X and from X to M but not from O to M. This partial band gap is sufficient for the designed resonator since the PnC needs to be reflective only in the resonant dimension, namely O to X. Since acoustic wave can propagate in the PnC structure when vibration frequency is outside the band gap, there will not be any spurious responses outside the band gap.

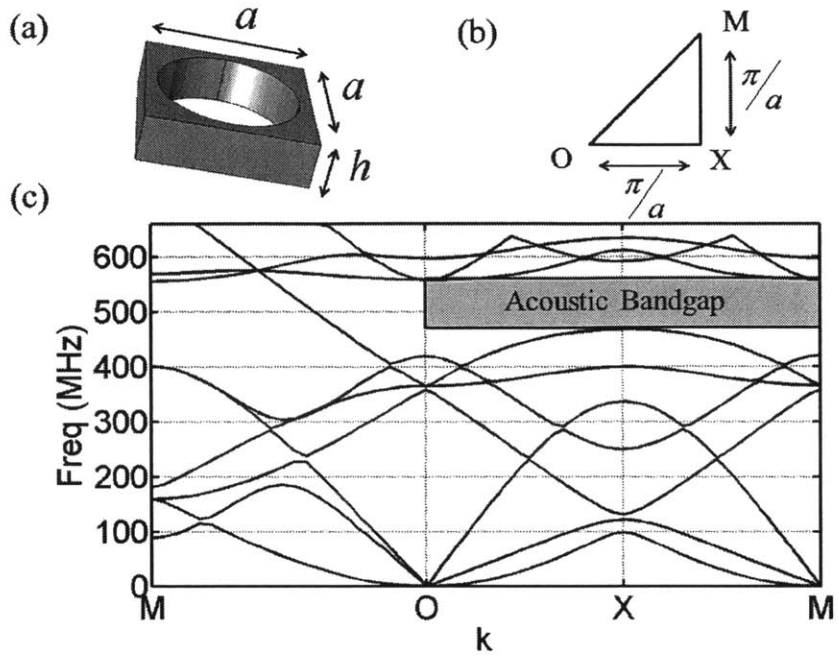

Figure 3-5: 3 types of PnC resonator configurations

While the PnC resonator inherently suppresses spurious modes outside the band gap, it was found that the majority of spurious modes found inside the band gap are due to harmonics established in the non-resonant dimension. Energy confinement along the non-resonant dimension must therefore be relaxed while maintaining high Q for the fundamental mode. These design considerations motivated the folded-PnC structure, in which square lattice PnC segments are designed at a folding angle θ relative to the main PnC to provide good confinement for the desired mode while minimizing standing waves formed in the non-resonant dimension.

3.4 Performance dependence on folding angle θ

Using 3D finite element method (FEM) simulations in COMSOL, folded PnC resonators with varying folding angle θ were investigated for their quality factor and spurious-free frequency range (SFFR). In these devices, Q is limited by acoustic losses to the substrate. To capture this loss in the FEM simulation, Perfectly Matched

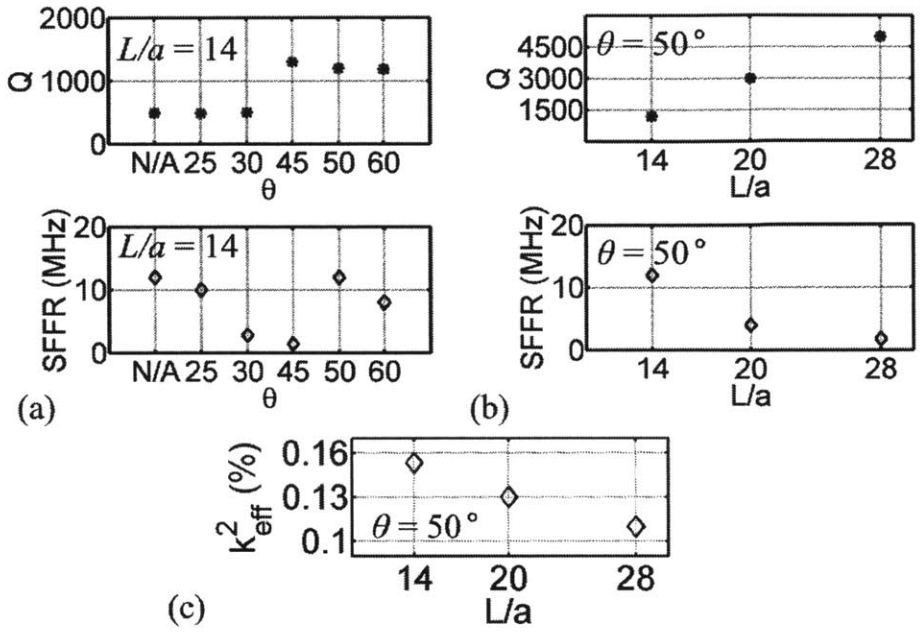

Figure 3-6: COMSOL simulated resonator performance, including Q, spurious-free frequency range (SFFR), and resonator coupling coefficient $k^2_{eff}$for varying PnC folding angle θ and cavity length L, normalized to the PnC unit cell length ($a = 5.6\mu m$ at 537 MHz).

Layers (PMLs) were implemented on the perimeter of the device beyond the PnC. Simulations included Multiphysics piezo-electric transduction to determine the 1-port response of the resonator. Q and SFFR were then extracted from a multi-pole fit to the 1-port admittance of the resonator. Simulated results of the angular dependence of Q and SFFR are shown in Fig. 3-6(a), where the angle θ = N/A corresponds to a PnC resonator of length L with completely open boundaries in the non-resonant dimension (no folded PnC segments). The simulated GaN resonator with interdigitated trans-ducer (IDT) has a 7th harmonic S0 Lamb mode around 537 MHz, using a PnC unit cell length of $a = 5.6\mu m$. A constant folded segment length of 5 unit cells was chosen for this design. The PnC band gap is established between 467 and 562 MHz.

As can be seen in Fig. 3-6(a), the presence of the folded PnC improves Q by a factor of over 2 above a critical angle between 30-45°, but tends to introduce spurious modes near the desired resonance. This can be explained by the role of the folded

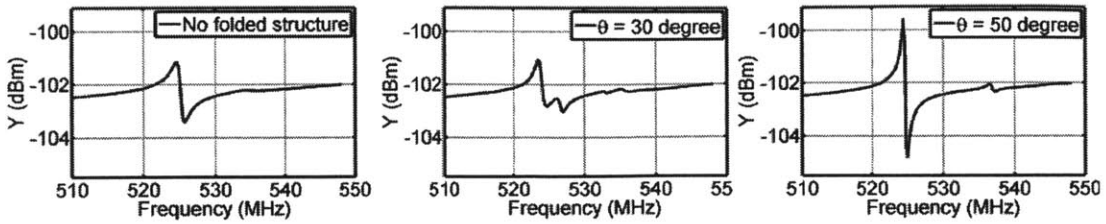

Figure 3-7: Spurious modes at different folding angle θ. $\theta = 50°$ does not introduce any additional anharmonic spurious response.

PnC segments in reflecting some radiated energy from the openings for all frequencies within the band gap, providing high Q for the fundamental mode but enabling standing waves orthogonal to the resonance which result in additional modes within the band gap. At all angles of the folded PnC segments, and even in the limiting case where no folded segments exist (θ = N/A), undesired harmonic modes along the non-resonant dimension are established due to the finite length of the PnC and driving electrodes which results in a break in translational symmetry. As already shown, Fig. (3-4) plots the 1-port frequency response of a simulated folded PnC resonator and the mode shapes of its main resonance and spurious modes. A device with longer cavity length ($L/a = 28$) is chosen for better illustration of harmonics in the non-resonant dimension and the two spurious modes established within the band gap correspond to the 3^{rd} and 5^{th} harmonics. Even harmonics are suppressed due to symmetry of the driving and sensing electrodes. For a fundamental mode frequency f_1 centered in the band gap, the frequency of the n_{th} harmonic spurious mode can be approximated to first order by

$$f_n = \sqrt{f_o^2 + \left(\frac{nv}{L}\right)^2} \tag{3.1}$$

where v is the wave velocity along the non-resonant dimension and f_0 is the resonance frequency of the S_0 Lamb mode in the case when cavity length L is infinite. As can be seen in Fig. (3-4), these harmonics are significantly attenuated relative to the fundamental mode. This attenuation is attributed to signal cancellation in the IDT and to the openings designed on the central axis of the folded PnC structure,

which not only route the transducer signal to the resonant cavity, but also relax energy confinement for waves traveling in the non-resonant dimension. At certain folding angles, additional anharmonic spurious modes not predicted by (3.1) arise due to scattering off the "defect" at the folding point of the PnC. The folding structure can be treated as a interruption of the translational symmetry of the square lattice or a "defect". It is found from FEM simulation that at $\theta = 50°$, these spurious modes are entirely suppressed, achieving SFFR comparable to the case of no folded segments (θ = N/A). This is illustrated in Fig. 3-7.

Moreover, at $\theta = 50°$ resonator Q is twice as high as that of the resonator without folded segments. Hence, this folding angle was selected for all designs in this work.

3.5 Performance dependence on cavity length L

A similar trade-off exists between Q and SFFR as a function of cavity length L, which also strongly affects resonator k_{eff}^2. Simulation results of this dependence are presented in Fig. 3-6(b) and (c). As L increases, resonator volume and therefore total stored energy increase. Meanwhile, energy loss is dominated by radiative losses at the PnC openings on the resonator's central axis, which only depends on aperture size and local energy density. Thus, for a given folding angle and folded PnC aperture at the openings, the ratio between stored energy and energy loss increases with L leading to a higher Q. A larger L also leads to smaller SFFR since increasing L brings spurious modes closer to the main peak, consistent with (3.1). On the other hand, shorter resonators will have spurious modes pushed to higher frequencies, causing those modes to be more attenuated as they are closer to the PnC band gap edge. For a short enough cavity, spurious modes can even be pushed outside the PnC band gap and become significantly attenuated, potentially eliminating all spurious modes inside the band gap. However, such design requires very small L, resulting in a reduced Q of the fundamental mode and increased motional impedance. The decrease in $k_{eff}^2$with increasing L (Fig. 3-6(c)) is mainly a side-effect of the increase in Q. For the same IDT transducer configuration, scaling the cavity length L does not affect C_m/C_o, where

C_m is the motional capacitance of the resonator and C_o is the nominal capacitance of the transducer as defined in Chapter 2, since both the mode and electrodes extend equally with L in the non-resonant dimension. When $Q\ C_o/C_m$, the series and parallel resonance of the mode shift apart, making k_{eff}^2larger than C_m/C_o. As Q increases, the two resonances move closer together, decreasing k_{eff}^2, which approaches C_m/C_o when $Q(C_m/C_o) >> 1$. For the devices in this work, $Q(C_m/C_o)\ 0.5 - 1$, a regime where the trade-off between Q and k_{eff}^2still exists. Consequently, the increase in Q corresponding to increased cavity length L leads to a drop in k_{eff}^2, as observed in simulation.

Chapter 4

Experimental Results and Analysis

4.1 Fabrication

As in any other MEMS project, it is fabrication that brings a design to life. Thanks to Laura Pope's hard work, I am able to test these PnC resonator designs. All the fabrication and SEM images involved in this thesis were done by Laura.

Folded PnC resonators were fabricated in MIT's Microsystems Technology Lab (MTL) using Raytheon's MMIC GaN-on-Si heterostructure, comprised of AlGaN(25 nm)/GaN(1.7 μm) grown on (111)-Si using Molecular Beam Epitaxy (MBE). A shallow AlGaN etch was used to remove the 2D electron gas (2DEG) between the AlGaN/GaN layers and allow for transduction in the GaN layer. A 100 nm layer of Ni (used as the gate metal for GaN HEMTs) was then deposited and patterned to define piezoelectric IDTs. The choice of Ni for the electrodes is a departure from conventional Au electrodes found in GaN MMICs, as Au is mechanically lossy and is known to reduce resonator Q. Since these devices are processed side by side with GaN HEMTs, a PECVD Si_3N_4 layer (150 nm) was deposited to passivate the surface and protect the 2DEG channel. A deep Cl_2 GaN etch then defined the PnCs and thus the acoustic cavities. Metal pads (50 nm Ti/300 nm Au) were then connected to the gate electrodes through vias in the passivation layer. Finally, a XeF_2 etch released the resonators from the Si substrate. Fig. 4-1 depicts the cross section of the final suspended resonator. An SEM of one of the fabricated PnC resonators (De-

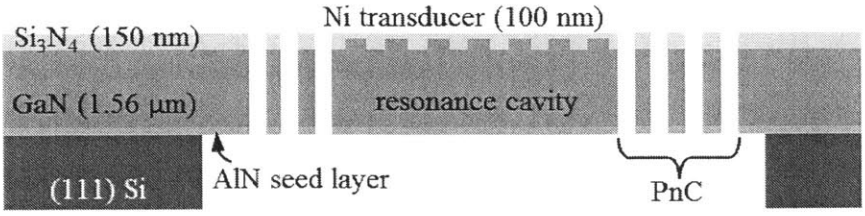

Figure 4-1: Cross section of MBE GaN resonator on Si.

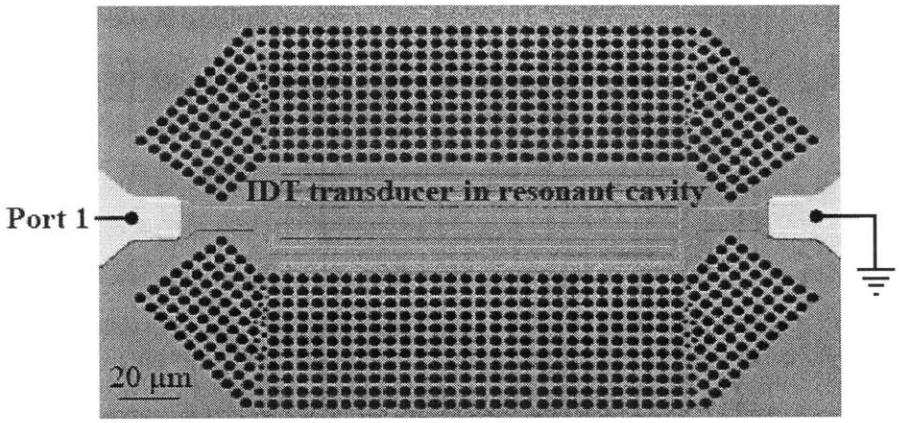

Figure 4-2: SEM of Device 1. IDT transducers (Ni) are routed into the resonant cavity through the openings. It is connected through vias to the probe pads, which are made of Au/Ti.

vice 1) is shown in Fig. 4-2, with cavity length L of 157 μm, folding angle $\theta = 50°$ and resonance at 516 MHz. This fabrication process is compatible with GaN HEMT technology [8].

4.2 Frequency Response and Analysis

Devices were tested under vacuum in a Cascade PMC200 RF probe system. A standard 1-port S-parameter measurement was performed using an Agilent 5225A Network Analyzer with on-chip open de-embedding structure up to the routing electrodes outside the cavity. The measured 1-port device admittance was fitted to a modified Butterworth-Van Dyke circuit to extract resonance parameters, with a shunt capacitor and resistor used to model the feed-through. We compare the performance of two devices with resonant dimension defined based on the structure in the simulation in

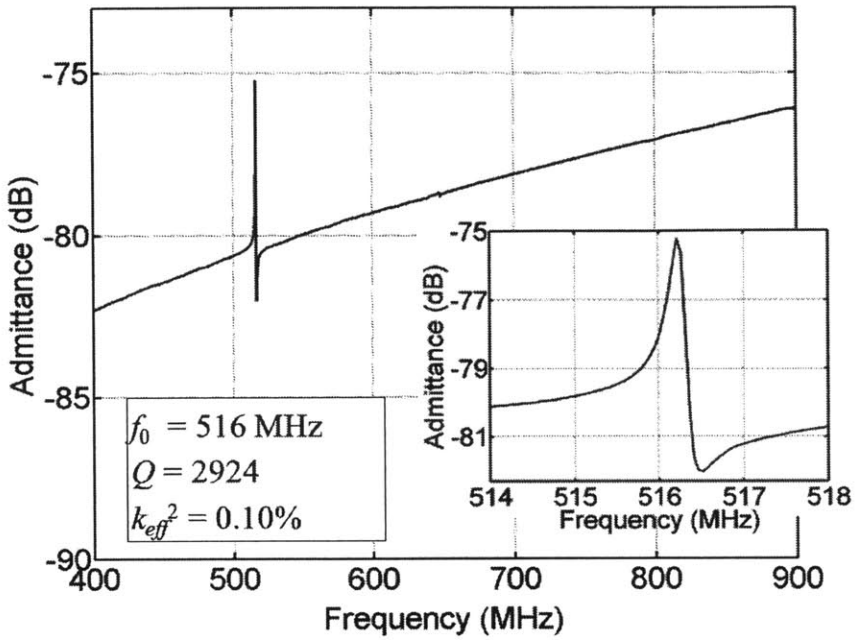

Figure 4-3: Measured frequency response of Device 1 with wide and narrow sweeps showing spurious-free spectrum.

	θ	a(μm)	L/a	f_0 (MHZ)	R_M (kΩ)	Q	k_{eff}^2
Dev1	50°	5.6	28	516	10	2924	0.10%
Dev2	50°	5.6	14	528	30	1160	0.23

Table 4.1: Measured performance comparison of GaN folded PnC resonators

Fig. 3-4 to demonstrate the behavior and design trade-offs of the folded PnC resonator. Labeled "Device 1" and "Device 2", the parameters of these resonators are provided in Table 4.1.

Fig. 4-6 shows the wide-band and zoomed in (inset) frequency response of Device 1, exhibiting a clean spectrum over >750 MHz range. Device 2 is identical apart from its cavity length, which is half that of Device 1. The 1-port frequency response of Device 2 is shown in Fig. (4-4). Reducing the cavity length by 2× decreases Q by 2.5× but improves $k_{eff}^2$by 2.3×. This trend is in accordance with simulation (Fig. 3-6) in which a 4× decrease and 1.6× increase are expected for the same length scaling for Q and k_{eff}^2, respectively.

In the interest of scaling to higher frequency, a third folded PnC resonator (Device

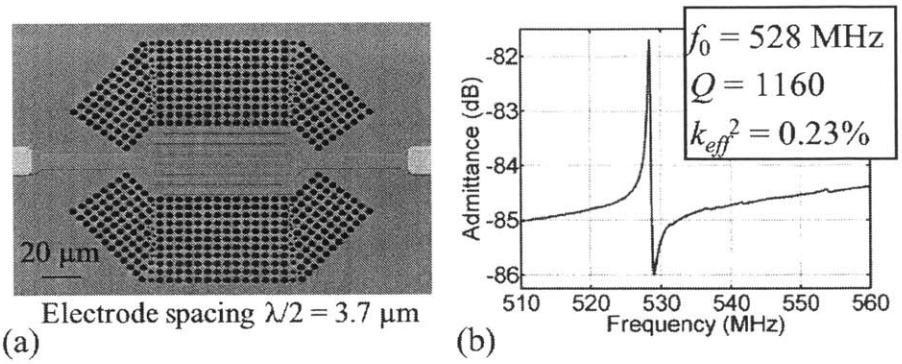

Figure 4-4: (a) SEM of Device 2, with $L/a = 14$. (b) Measured 1-port frequency response and fitted resonator parameters.

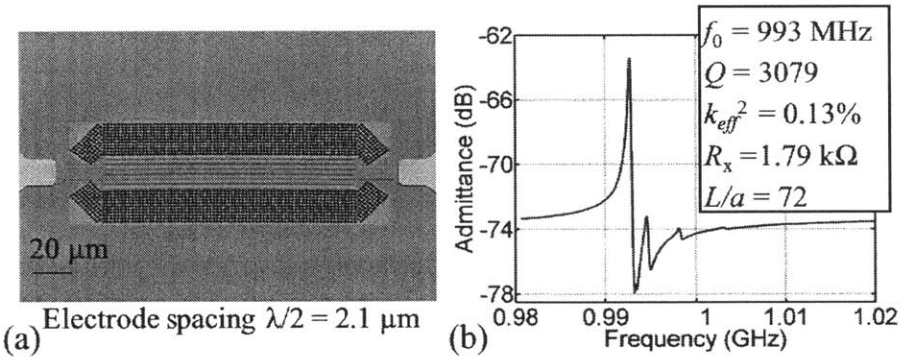

Figure 4-5: SEM of Device 3 at 993 MHz ($a = 2.3\mu m$) (b) Measured 1-port frequency response and fitted resonator parameters.

3) was demonstrated at 993 MHz, achieving an $f \cdot Q$ product of 3.06×10^{12}. The PnC used for Device 3 has a band gap of from 940 to 1040 MHz. The SEM, frequency response, and fitted parameters for this structure are shown in Fig. 4-5. The harmonic spurious modes described by 3.1 can be seen more clearly in Device 3, since the frequency difference between the fundamental mode and the first spurious mode is the same as in the case of Devices 1 and 2, but at 993 MHz the fractional difference is smaller. Table 4.2 lists fundamental resonance frequency, spurious frequencies and their spacings. It can be seen that $\Delta f_{23} = 2\Delta f_{12}$ and $\Delta f_{35} = 2\Delta f_{13}$, consistent with the prediction based on (3.1). The 2nd harmonic spurious mode in this device appears due to slight misalignment of the IDT electrodes.

f_1	f_2	f_3	f_5	f_7
992.7	993.3	994.5	998.1	1003.1
Δf_{12}	Δf_{23}	Δf_{13}	Δf_{35}	Δf_{57}
0.6	1.2	1.8	3.6	5.0

Table 4.2: Spurious modes frequencies and spacings in Device 3.

4.3 Nonlinearity and IIP3

Finally, an IP3 measurement was performed on Device 3 to characterize the device's power handling capability, a critical metric for filter applications. Two interfering tones with same power, spaced at 300 kHz and 600 kHz, were combined to drive the resonator. At the output, the signal at the resonant frequency was detected due the 3rd order nonlinearity of the device. Measurement results and calculated IIP3 are shown in Fig. 10. Input power has been calibrated to represent the power incident onto the device input port. The folded structure PnC resonator exhibits IIP3 of +27.2 dBm, the highest reported in a GaN resonator to date. This is attributed to improved thermal conductance offered by the PnC boundaries relative to tethered structures.

The actual measurement setup is more involved than simply applying the two off-resonance frequencies, since it is practically impossible to align the mixed signal perfectly with the resonance. A stable frequency source is set at $f_o - 2\Delta f$ to provide one of the two interfering signal. The other one is provided through a frequency sweep centered at $f_o - \Delta f$ at the same power level using VNA. Before feeding both either signals to the mixture whose output then drives the resonator, a low pass filter with a cut off frequency between f_o and $2f_o$ is applied to both signals. The purpose for the low pass filter is to eliminate the second and above harmonics contained in the interfering signal. Since these harmonics in the interfering signal may also mix with each other and index nonlinearity frequency components at the resonance, thus affecting the accuracy of IIP3 measurement, which characterizes the 3^{rd} order nonlinearity of the Device Under Test (DUT) under two pure interfering signals. At the sensing port of the resonator, a spectrum analyzer is used to detect the various frequency components contained in the sensed signal. The alignment of the IM3 signal peak and the resonance frequency is detected by operating the spectrum analyzer in

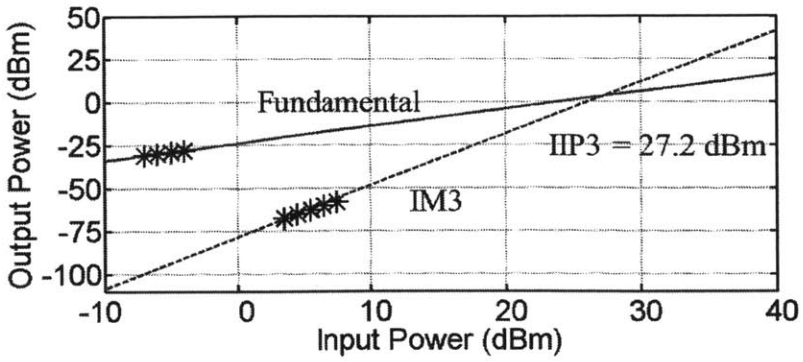

Figure 4-6: Cross section of MBE GaN resonator on Si.

MAX HOLD mode. The peak value of the IM3 signal when the alignments happens is used as for extrapolating the IM3 line in the output power vs input power plot.

There are two main sources of nonlinearity, thermal and vibration amplitude.

- Thermal effects cause resonator nonlinearity, since temperature will affect the stiffness and piezoelectric coefficient, leading to changes in resonator frequency and motional impedance.

- Linear piezo-electricity and stiffness are only valid for weak electric field and small displacement. High driving power level induces large vibration amplitude and strong electric field, leading to nonlinear resonator behavior.

4.4 Temperature Coefficient of Temperature

As mentioned, the potential for integrating GaN MEMS with GaN circuits is promising and can lead to many benefits for RF communication applications and among them, timing is an exciting domain. A thermally stable frequency source is crucial in using MEMS resonator for timing applications. We measured the Temperature Coefficient of Frequency for the PnC GaN resonator to be -23ppm/K. This is consistent with the intrinsic Temperature Coefficient of Elasticity (TCE) for GaN. One possible approach that we will explore is to use Silicon Oxide, which has an intrinsic positive TCE of +90ppm/K, to perform passive compensation for the GaN resonator.

Selecting the correct locations for passive compensation and optimizing compensation result under fabrication variation will be interesting topics to look at.

Chapter 5

Conclusion

We introduce a new RF MEMS resonator using a folded PnC structure to achieve wide band spurious mode suppression. The usage of Gallium Nitride fabrication technology that is compatible with HEMT process and the usage of Phononic Crystal for wide band spurious mode suppression are the two main unique innovations this work brings to the field. Devices show clean frequency response over a wide bandwidth (>500MHz). At 993 MHz, high $f \cdot Q$ product of 3.06×10^{12} was demonstrated, on par with the best results in GaN to date. Furthermore, the device exhibited large power handling of over +27 dBm potentially afforded by improved thermal dissipation in the large-perimeter PnC. This design leverages GaN MMIC technology, providing a low barrier-to-entry solution for monolithic timing and RF wireless communication applications including GHz MEMS front end band pass filters with excellent spurious mode suppression, linearity, and frequency selectivity.

Applying acoustic meta-materials such as Phononic Crystal on Gallium Nitride material platform to improve MEMS resonator performance will be the focus of my future study in the PhD. Better understanding on the Temperature Coefficient of Frequency, nonlinearity of GaN MEMS resaontors, eliminating the releasing step by making the resonator attached to the substrate will be interesting topics to look into. Optimizing the PnC design for better quality factor and cleaner spectrum, and using PnC's nonlinear band structure to manipulate acoustic wave can potentially introduce brand new concepts and design into the field of MEMS resonators.

Bibliography

[1] M. Giovannini, S. Yazici, Nai-Kuei Kuo, and G. Piazza. Spurious mode suppression via apodization for 1 ghz aln contour-mode resonators. In *Frequency Control Symposium (FCS), 2012 IEEE International*, pages 1–5, May 2012.

[2] Chao-Yi Huang, Jia-Hong Sun, and Tsung-Tsong Wu. A two-port zno/silicon lamb wave resonator using phononic crystals. *Applied Physics Letters*, 97(3):031913–031913–3, Jul 2010.

[3] Steven G. Johnson John D. Joannopoulos and Joshua N. Winn. *Photonic Crystals: Molding the Flow of Light.* Princeton University Press, 2008.

[4] Ville Kaajakari. *Practical MEMS.* Small Gear Publishing, 2009.

[5] N. Kuo, S. Gong, and G. Piazza. Ultra high frequency phononic crystal in silicon carbide. In *Solid-State Sensors, Actuators and Microsystems Conference (TRANSDUCERS), 2011 16th International*, pages 2486–2489, June 2011.

[6] Saeed Mohammadi and A. Adibi. Waveguide-based phononic crystal micro/nanomechanical high- q resonators. *Microelectromechanical Systems, Journal of*, 21(2):379–384, April 2012.

[7] Saeed Mohammadi, Ali Asghar Eftekhar, W.D. Hunt, and Ali Adibi. High-q micromechanical resonators in a two-dimensional phononic crystal slab. *Applied Physics Letters*, 94(5):051906–051906–3, Feb 2009.

[8] L.C. Popa and D. Weinstein. Switchable piezoelectric transduction in algan/gan mems resonators. In *Solid-State Sensors, Actuators and Microsystems (TRANS-*

DUCERS EUROSENSORS XXVII), 2013 Transducers Eurosensors XXVII: The 17th International Conference on, pages 2461–2464, 2013.

[9] Philip Jason Stephanou. Piezoelectric aluminum nitride mems resonators for rf signal processing, 2006.

[10] M. F. Su, R.H. Olsson, Z.C. Leseman, and El-Kady. Realization of a phononic crystal operating at gigahertz frequencies. *Applied Physics Letters*, 96(5):053111–053111–3, Feb 2010.